STRUCTURAL BIOLOGY COMMUNICATIONS

ISSN 2053-230X

Structural characterization of *Porphyromonas gingivalis* enoyl-ACP reductase II (FabK)

Kirk E. Hevener,[a,b]* Bernard D. Santarsiero,[b] Hyun Lee,[b] Jesse A. Jones,[a] Teuta Boci,[b] Michael E. Johnson[b] and Shahila Mehboob[b,c]*

[a]Department of Pharmaceutical Sciences, University of Tennessee Health Science Center, 881 Madison Avenue, Suite 571, Memphis, TN 38163-2198, USA, [b]Center for Pharmaceutical Biotechnology, University of Illinois at Chicago, 900 South Ashland Avenue, Suite 3100, Chicago, IL 60607-7173, USA, and [c]Novalex Therapeutics, Chicago, IL 60612, USA. *Correspondence e-mail: khevener@uthsc.edu, shahila@gmail.com

Received 13 October 2017
Accepted 4 January 2018

Edited by S. Sheriff, Bristol-Myers Squibb, USA

Keywords: *Porphyromonas gingivalis*; periodontal disease; enoyl-ACP reductase II; FabK; crystal structure.

PDB reference: *Porphyromonas gingivalis* enoyl-ACP reductase II (FabK) with cofactors NADPH and FMN, 4iql

Supporting information: this article has supporting information at journals.iucr.org/f

Enoyl-acyl carrier protein (ACP) reductase II (FabK) is a critical rate-limiting enzyme in the bacterial type II fatty-acid synthesis (FAS II) pathway. FAS II pathway enzymes are markedly disparate from their mammalian analogs in the FAS I pathway in both structure and mechanism. Enzymes involved in bacterial fatty-acid synthesis represent viable drug targets for Gram-negative pathogens, and historical precedent exists for targeting them in the treatment of diseases of the oral cavity. The Gram-negative organism *Porphyromonas gingivalis* represents a key causative agent of the costly and highly prevalent disease known as chronic periodontitis, and exclusively expresses FabK as its enoyl reductase enzyme in the FAS-II pathway. Together, these characteristics distinguish *P. gingivalis* FabK (*Pg*FabK) as an attractive and novel narrow-spectrum antibacterial target candidate. *Pg*FabK is a flavoenzyme that is dependent on FMN and NADPH as cofactors for the enzymatic reaction, which reduces the enoyl substrate *via* a ping-pong mechanism. Here, the structure of the *Pg*FabK enzyme as determined using X-ray crystallography is reported to 1.9 Å resolution with endogenous FMN fully resolved and the NADPH cofactor partially resolved. *Pg*FabK possesses a TIM-barrel motif, and all flexible loops are visible. The determined structure has allowed insight into the structural basis for the NADPH dependence observed in *Pg*FabK and the role of a monovalent cation that has been observed in previous studies to be stringently required for FabK activity. The *Pg*FabK structure and the insights gleaned from its analysis will facilitate structure-based drug-discovery efforts towards the prevention and treatment of *P. gingivalis* infection.

1. Introduction

Periodontitis is a polymicrobial-associated inflammatory disease that causes the destruction of bone and tooth-supporting tissues. It is the major cause of tooth loss in the world and is associated with a high global burden in terms of treatment and preventative costs (Schaudinn *et al.*, 2009; Snowden *et al.*, 2003). The bacterial species *Porphyromonas gingivalis* is associated with particularly aggressive, chronic disease that is often resistant to standard treatments (Lovegrove, 2004; Chávarry *et al.*, 2009; Fitzpatrick & Katz, 2010; Joshipura *et al.*, 2009). Additionally, recent studies have revealed *P. gingivalis* to be a 'keystone' species in periodontal disease that is able to modulate the host immune response, allowing other pathogenic species to thrive (Hajishengallis *et al.*, 2011). These studies have suggested that specific antimicrobial therapy directed toward *P. gingivalis* may have a strong clinical impact on community-wide oral health. Because *P. gingivalis* is frequently resistant to standard treatments, the development of novel treatments targeting previously unexploited pathways is critically needed.

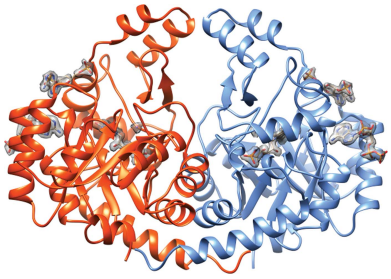

One attractive, yet largely undeveloped, area of antibacterial development is the bacterial type II fatty-acid synthesis (FAS II) pathway. This pathway is distinct from that in mammals and has been shown to be essential in Gram-negative bacteria and some Gram-positive bacteria, which makes it an appealing and potentially selective antibacterial target (Gerusz, 2010; Kingry *et al.*, 2013). Although novel, the use of agents targeting the FAS II pathway in the prevention and treatment of periodontal disease is not entirely without precedent. The antibacterial triclosan, which is a known inhibitor of FabI (enoyl-ACP reductase I), has been used as a component of oral hygiene products in the past (Blinkhorn *et al.*, 2009; Vered *et al.*, 2009). *P. gingivalis* expresses an isozyme of FabI, FabK (enoyl-ACP reductase II), which is responsible for a key rate-limiting reduction step in the synthesis of bacterial fatty acids (Fig. 1). Additional enoyl-reductase isozymes which are known to be selectively expressed in bacteria are FabL and FabV (enoyl-ACP reductases III and IV, respectively). Some bacteria are known to co-express multiple enoyl reductase isozymes, including *Enterococcus faecalis*, which expresses FabI and FabK, and *Pseudomonas aeruginosa*, which expresses FabI, FabL and FabV. However, the FabK enzyme is the sole isozyme in *P. gingivalis* and is completely resistant to triclosan and other FabI-active agents (Marrakchi *et al.*, 2003). Although the existence of multiple isozymes at this step in the pathway precludes the possibility of developing broad-spectrum antimicrobials, a possibility exists that relatively selective antibacterial agents may be developed that can target harmful bacterial species such as *P. gingivalis* while avoiding activity against so-called 'beneficial bacteria'.

The FabK enzyme from *Streptococcus pneumoniae* (*Sp*FabK) has previously been characterized (Marrakchi *et al.*, 2003) and structures, both apo and with a known inhibitor bound, have been determined for this enzyme, leading to several key observations (Saito *et al.*, 2006, 2008). *Sp*FabK is a flavoenzyme that is dependent upon an FMN prosthetic group and an NADH cofactor, and uses a ping-pong, bi-bi enzyme mechanism to reduce the enoyl substrate (Hevener *et al.*, 2012; Saito *et al.*, 2008). *Sp*FabK is structurally distinct from FabI (as well as FabV and FabL) and possesses an overall triosephosphate isomerase (TIM) barrel structural fold, whereas FabI, FabV and FabL fall within the short-chain dehydrogenase/reductase (SDR) superfamily of reductases and possess a classical Rossmann fold for binding to their NAD(P)H cofactor (White *et al.*, 2005; Oppermann *et al.*, 2003). Interestingly, an intrinsic NADH oxidation activity, in the absence of enoyl substrate, has been reported for *Sp*FabK (Marrakchi *et al.*, 2003). The significance of this activity is unclear, but it was hypothesized that FabK is related to bacterial NADH oxidases involved in the anaerobic catabolism of glucose (Marrakchi *et al.*, 2003). Lastly, the activity of the *Sp*FabK

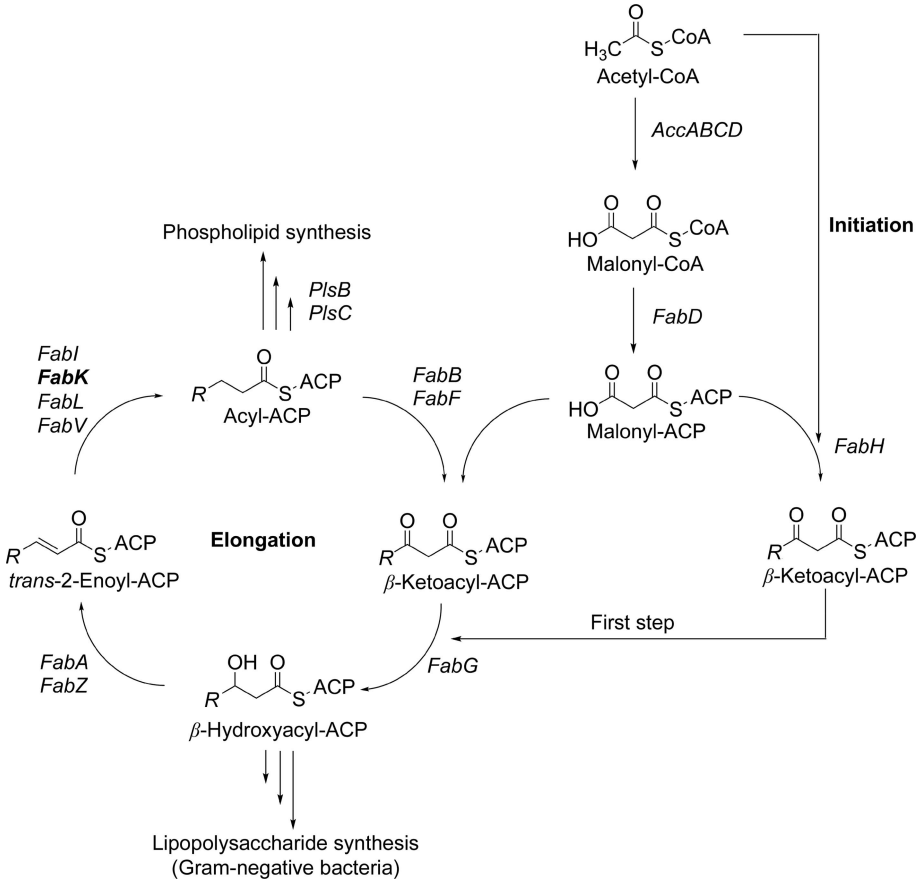

Figure 1
Bacterial FAS-II pathway. Adapted with permission from Gerusz *et al.* (2012), *J. Med. Chem.* **55**, 9914–9928. Copyright 2012 American Chemical Society.

enzyme was shown to be critically dependent on monovalent cation salts, and a preference for NH_4^+ salts was observed with respect to the potentiation of activity. No activity was seen with the use of bivalent cation salts, and removal of the monovalent salts resulted in an apparent loss of the structural integrity of the enzyme (Marrakchi *et al.*, 2003).

We have previously reported preliminary kinetic characterization and crystallization studies of *P. gingivalis* FabK (*Pg*FabK; Hevener *et al.*, 2012). *Pg*FabK has 41% overall sequence identity to *Sp*FabK. Unlike the preference of *Sp*FabK for NADH, *Pg*FabK showed a strong preference for NADPH. K_m values for both NADPH and the enoyl substrate crotonyl-CoA have been determined and balanced assay conditions were reported. We also noted a slight, intrinsic NADPH oxidation with *Pg*FabK in the absence of substrate, and interestingly the enzyme kinetics suggested a pattern of substrate inhibition at higher concentrations of NADPH (Hevener *et al.*, 2012). However, several critical issues still impede successful structure-based design efforts towards the identification of *Pg*FabK inhibitors. Firstly, the binding mode of the NADPH/$NADP^+$ cofactor has not been established, nor has the structural basis for the dependence of *Pg*FabK on NADPH over NADH been established. Secondly, missing loop elements in the crystal structures of *Sp*FabK only allow partial visualization of the active site. Lastly, the structural basis for the cation dependence and the intrinsic activity that has been noted has not been established. Here, we report the structure of *Pg*FabK determined to 1.9 Å resolution using X-ray crystallography. In this structure, all flexible loops are present surrounding the active site. Additionally, the endogenous FMN prosthetic group is fully visible and the NADPH cofactor is partially resolved in two distinct binding sites. A metal-binding pocket in the active site is clearly occupied by a sodium ion and provides insights into the structural basis for the cation dependence that has been noted.

2. Materials and methods

2.1. Reagents, chemicals, biologicals and equipment

The protein-expression cell line *Escherichia coli* BL21-Gold (DE3) was obtained from Agilent Technologies, Santa Clara, California, USA (catalog No. 230132). The pET-15b plasmid vector was obtained from Novagen/Millipore, Madison, Wisconsin, USA. Genomic DNA (*P. gingivalis* strain W83; BAA-308D-5) was obtained from ATCC, Manassas, Virginia, USA. Oligonucleotide primers were obtained from Integrated DNA Technologies (IDT), Coralville, Iowa, USA. The Ni-IMAC column (HisTrap HP, 5 ml) and gel-filtration columns (HiLoad 26/600 and 16/600, Superdex 200 pg) were obtained from GE Healthcare, Piscataway, New Jersey, USA. Ampicillin, isopropyl β-D-1-thiogalactopyranoside (IPTG) and β-nicotinamide adenine dinucleotide 2′-phosphate reduced tetrasodium salt (NADPH) were obtained from Sigma–Aldrich Chemicals, St Louis, Missouri, USA. Crystallization screening kits (SaltRx, Index, Crystal Screen and PEG/Ion) and supplies were obtained from Hampton Research, Aliso Viejo, California, USA. The expression media LB and TB broth (BD Difco), MOPS buffer and NaCl (Acros Organics), and glycerol (Fisher Chemical) were obtained from Fisher Scientific, Pittsburgh, Pennsylvania, USA.

Table 1
Macromolecule-production information.

Source organism	*P. gingivalis* strain W83 (BAA-308D-5)
DNA source	gDNA
Forward primer	5′-GAA TAA GCA TAT GAA TAG AAT TTG CGA ATT ATT GGG T-3′
Reverse primer	5′-AGA TGG ATC CTC ATA TCT CAG TGG G-3′
Cloning vector	pET-15b
Expression vector	pET-15b
Expression host	*E. coli* BL21 (DE3)
Complete amino-acid sequence of the construct produced	MGSSHHHHHHSSGLVPRGSHMNRICELLGI EHPIISGGMVWCSGWKLASAVSNCGGLG LIGAGSMHPDNLEHHIRSCKAATDKPFG VNVPLLYPEMDKIMEIIMREHVPVVVTS AGSPKVWTAKLKAAGSKVIHVVSSATFA RKSEAAGVDAIVAEGFEAGGHNGREETT TLCLIPEVVDAVNIPVVAAGGIASGRAV AAALALGADAVQVGTRFALSEESSAHED FKAHCRRSVEGDTMLSLKAVSPTRLLKN KFYQDVFAAEQRGASVEELRELLGRGRA KQGIFEGDLHEGELEIGQAVSQISHAET VAEIMVDLVDGYKRSLAGMPTEI

2.2. Macromolecule production

We have previously reported the cloning, expression and purification of FabK from *P. gingivalis* (Hevener *et al.*, 2012). In brief, a standard prokaryotic protein-expression protocol was used to express the *Pg*FabK enzyme. The *fabK* gene was cloned by PCR amplification using genomic DNA from the W83 strain of *P. gingivalis*. Primers were designed in-house and ordered from a commercial source (Table 1). The gene was cloned into the BamHI and NdeI restriction sites of pET-15b. After sequence confirmation, *E. coli* strain BL21 (DE3) was used for the expression of *Pg*FabK. The expressed protein was purified using two chromatographic steps: an immobilized metal-affinity (IMAC) step using nickel-chelating resin followed by size-exclusion chromatography. FMN was co-purified along with the target protein and was not supplemented during the expression or purification stages. The typical yield is approximately 20 mg protein per litre of culture medium, with greater than 95% purity. The His tag was not removed and all studies reported here involved the use of affinity-tagged protein.

2.3. Crystallization

Protein crystals were grown using the hanging-drop vapor-diffusion method. A coarse-matrix screen was employed using commercially available kits to identify preliminary crystallization conditions. The protein was incubated for 15 min at room temperature with a tenfold molar excess of NADPH prior to crystallization setup. The initial crystal-growth conditions were 0.15 *M* sodium citrate pH 5.6, 10% PEG 3350, 5 mg ml^{-1} protein in drops consisting of a 1:1 ratio of protein solution and well buffer (Table 2). Crystals were visible within one week.

Table 2
Crystallization.

Method	Vapor diffusion, hanging drop
Plate type	24-well VDX plate with sealant (Hampton Research)
Temperature (K)	291
Protein concentration (mg ml^{-1})	5
Buffer composition of protein solution	Initial: 10 m*M* MOPS pH 7.5, 100 m*M* NH_4Cl, 1.4 m*M* NADPH, 5 m*M* DTT Microseeding: 0.15 *M* sodium citrate pH 5.6, 10%(*w*/*v*) PEG 3350
Composition of reservoir solution	Initial crystal: 0.15 *M* sodium citrate pH 5.6, 10% PEG 3350 Microseeding: 0.2 *M* sodium formate pH 7.0, 20% PEG 3350
Volume and ratio of drop	3 µl protein stock:3 µl Index condition No. 90:1 µl seed stock (seed stock from 10% PEG 3350, 0.15 *M* sodium citrate pH 5.6)
Volume of reservoir (µl)	500

2.3.1. Microseeding. Crystals were harvested from the initial hit condition, looped through 50% glycerol (with well buffer) for cryoprotection and screened for their ability to diffract X-rays using an in-house X-ray diffractometer. Because they diffracted poorly, a series of microseeding trials were undertaken using the initial protein crystals to generate seed stocks and rescreen. This technique resulted in the identification of a novel crystallization condition (0.2 *M* sodium formate pH 7.0, 20% PEG 3350) that resulted in crystals with significantly better diffraction compared with the initial conditions.

2.4. Data collection and processing

*Pg*FabK crystals were harvested, looped through 50% glycerol for cryoprotection and cooled to 100 K for data collection. A complete data set was collected on LS-CAT beamline 21-ID-F at Sector 21 of the Advanced Photon Source, Argonne National Laboratory, Lemont, Illinois, USA (Table 3). The data were processed using *XDS* and scaled with *XSCALE* (Kabsch, 2010*a*,*b*).

2.5. Structure determination and refinement

The structure of *Pg*FabK was determined *via* molecular replacement with *Phaser* from the *CCP*4 package (Winn *et al.*, 2011) using the previously reported *Sp*FabK structure (Saito *et al.*, 2006, 2008). Model refinement was performed using *REFMAC* and model building in *Coot* (Murshudov *et al.*, 2011; Emsley *et al.*, 2010; McCoy *et al.*, 2007). Restraint files for the FMN, NDP and GOL ligands were obtained from the CCP4 monomer library. The structure was validated using *MolProbity* (Chen *et al.*, 2010). Figs. 2, 4 and 5 were produced using the *UCSF Chimera* package (Pettersen *et al.*, 2004) from the Resource for Biocomputing, Visualization and Informatics at the University of California, San Francisco (supported by NIH P41 RR001081) and were rendered using *POV-ray* (Persistence of Vision Pty Ltd).

Table 3
Data collection and processing.

Values in parentheses are for the outer shell.

Diffraction source	Beamline 21-ID-F, APS
Wavelength (Å)	0.97
Temperature (K)	100
Detector	Rayonix MX-225 CCD
Crystal-to-detector distance (mm)	200.5
Rotation range per image (°)	1
Total rotation range (°)	360
Exposure time per image (s)	1
Space group	$P2_12_12_1$
a, *b*, *c* (Å)	48.65, 86.65, 150.51
α, β, γ (°)	90, 90, 90
Mosaicity (°)	0.1
Resolution range (Å)	20–1.938 (2.05–1.938)
Total No. of reflections	648327 (97141)
No. of unique reflections	90851 (14235)
Completeness (%)	99.5 (97.5)
Multiplicity	7.1 (6.8)
$\langle I/\sigma(I)\rangle$	15.2 (4.2)
$R_{\rm r.i.m.}$	0.145 (0.583)
Overall *B* factor from Wilson plot (Å^2)	21
$CC_{1/2}$	0.997 (0.892)

2.6. Analytical gel filtration

A HiLoad 16/600 Superdex 75 pg (120 ml, 16 × 600 mm) size-exclusion column was equilibrated at 277 K with one and a half column volumes (180 ml) of buffer *A* consisting of 10 m*M* MOPS pH 7.0, 50 m*M* NH_4Cl, 2 m*M* DTT at a flow rate of 1 ml min^{-1}. 3 ml of concentrated *Pg*FabK protein (at approximately 6 mg ml^{-1}) in buffer *A* was loaded onto the equilibrated column at a flow rate of 1 ml min^{-1}. Elution was performed over one column volume (120 ml), and the FabK protein eluted at an elution volume of around 60 ml. Three reference proteins with known molecular weights (94, 44 and 17 kDa) were also tested using the same column and flow rate.

3. Results and discussion

3.1. Overall structure of *Pg*FabK

The crystal structure of *Pg*FabK was determined to 1.94 Å resolution and refined to $R_{\rm work}$ and $R_{\rm free}$ values of 0.161 and 0.207, respectively. The structure contains two domains per 33 kDa monomer and includes a fully resolved endogenous FMN prosthetic group and a partially resolved NADPH cofactor, with all flexible loops fully visible. The bulk of each monomer is comprised of residues 1–198 of the N-terminal domain, which form eight alternating α-helix–β-strand repeats with the β-strands forming an internal core encompassed by the α-helices, making up a classic TIM-barrel motif (Fig. 2). The single FMN cofactor binds noncovalently atop the barrel near the C-terminal ends of the β-strands. Residues 198–289 comprise much of the C-terminal domain, forming a putative lid above the TIM barrel and containing a β-hairpin that resides proximal to the catalytic residue His143 (see below). Residues 290–308 form an additional α-helix adjacent to the TIM barrel. Six sodium ions, three associated with each chain, were modelled into the final structure (Table 4), with an average overall *B* factor of 20 Å^2. Sodium ions were selected

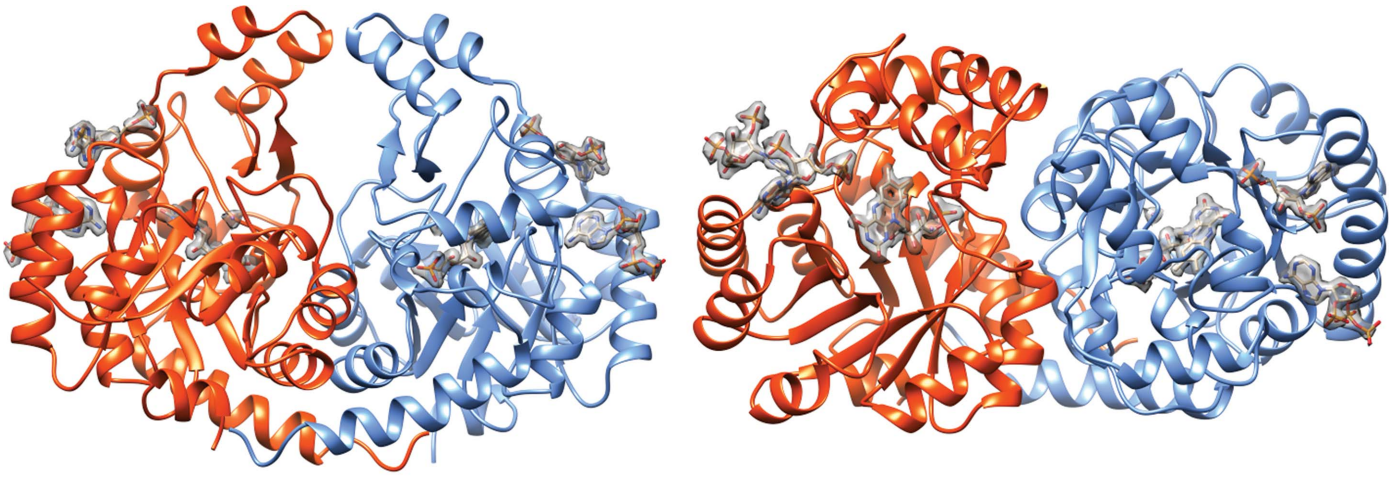

Figure 2
Overall *Pg*FabK structure. (*a*) *Pg*FabK enzyme depicted as the dimer (chain *A*, orange; chain *B*, blue). The FMN prosthetic group and NADPH cofactors are shown with density-contour maps. (*b*) Rotation of (*a*) by 90° about the *x* axis.

Table 4
Structure determination and refinement.

Values in parentheses are for the outer shell.

Resolution range (Å)	20.00–1.94 (1.988–1.938)
Completeness (%)	99.7
σ Cutoff	None
No. of reflections	
Working set	45527 (3152)
Test set	2424 (175)
Final R_{cryst}	0.161 (0.210)
Final R_{free}	0.207 (0.272)
Cruickshank DPI	0.151
No. of non-H atoms	
Protein	4638
Ion (Na^+)	6
Ligand (FMN)	62
Ligand (NDP)	116
Ligand (GOL)	6
Water	319
Total	5147
R.m.s. deviations	
Bonds (Å)	0.017
Angles (°)	1.6
Average *B* factors (Å^2)	
Protein	13
Ion (Na^+)	20
Ligand (FMN)	9.5
Ligand (NDP)	25
Ligand (GOL)	22
Water	18
Ramachandran plot	
Favored (%)	97.6
Allowed (%)	100.0

as initial attempts to place water molecules at these positions resulted in higher *B* factors and the coordinating geometry was consistent with metal ions rather than water molecules (Supplementary Fig. S1).

Several interactions exist between the N-terminal TIM-barrel β-strands and the FMN cofactor. The isoalloxazine-ring system of FMN forms hydrogen bonds to Asn68 and Ser94 and a backbone hydrogen bond to Val20, as well as interactions with several water molecules. The ribityl moiety of the FMN molecule forms hydrogen bonds to Glu136 and Gln190, in addition to forming a backbone hydrogen-bond interaction with Met19 and multiple water-molecule interactions. The C-terminal 'lid' domain appears to form a pocket between itself and the N-terminal domain, in which the phosphate from the FMN cofactor binds. Here, the phosphate moiety forms a hydrogen bond to Thr193 and backbone interactions with Gly171, Gly192 and Thr193, as well as making interactions with several water molecules.

Previously determined structures of *Sp*FabK and *Tm*FabK were consistent with a dimeric enzyme, but the functionality of the dimer was not confirmed. The *Pg*FabK homodimer interface buries an extensive surface area of about 2200 Å^2 involving 33 hydrogen bonds and nine salt bridges as calculated by the *PDBePISA* server (Krissinel & Henrick, 2007). Additionally, a favorable solvation-energy gain upon interface formation, estimated at −28.1 kcal mol^{-1}, indicates a high

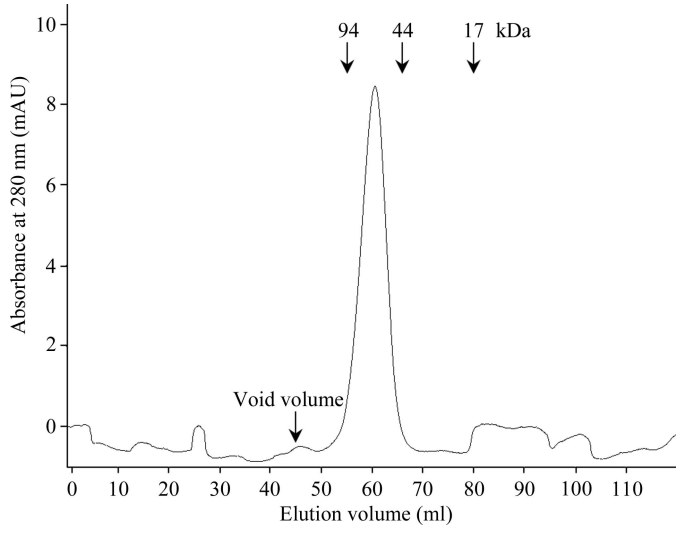

Figure 3
UV profile of gel filtration of *Pg*FabK. The protein-elution peak relative to the control proteins suggests a functional *Pg*FabK dimer (the monomer is 33 kDa).

probability that the enzyme is a functional dimer. This was further confirmed by investigating the oligomeric state of this enzyme in solution by size-exclusion chromatography. *Pg*FabK eluted between 94 and 44 kDa (Fig. 3), confirming a functional 66 kDa dimer. All of this is conclusively corroborated by the electron density and overall determined crystal structure showcasing the dimer.

3.2. Structural basis of NADPH dependence

While the FabK isozyme from *S. pneumoniae* was reported to be highly selective for NADH over NADPH as the nucleotide cofactor (Marrakchi *et al.*, 2003), we have observed the *P. gingivalis* FabK enzyme to show greater selectivity for NADPH (Hevener *et al.*, 2012). To elucidate the structural basis for these observations, the NADPH cofactor was co-crystallized with the FabK protein (see §2 above) using a tenfold molar excess of NADPH. The refined model shows the presence of two partially resolved NADPH molecules bound to each FabK monomer: one near the active site and one located distant from the active site. The second NADPH molecule is approximately 8.5 Å distant from the active-site NADPH molecule, with the adenine-ring system occupying a hydrophobic pocket created by Phe267, Trp21, His53, Met45 and Asn49. The presence of the second (adventitious) NADPH molecule is presumed to be a co-crystallographic artefact arising from the use of a tenfold molar excess of NADPH in the crystallization buffer. However, we note that the average *B* factor for the second NADPH molecule is slightly lower than that calculated for the NADPH molecule residing in the active site: 21 and 29 Å^2, respectively.

Both NADPH molecules are only partially resolved, with no visible electron density for the nicotinamide moiety past the diphosphate linker at an r.m.s.d. of 1 (Supplementary Figs. S2 and S3). This may be owing to hydrolytic cleavage of the nicotinamide group at the diphosphate moiety (Wu *et al.*, 1986) or structural disorder. A small deviation from the optimal value for the O1X—P2B—O3X angle (119.9° with standard deviation of 3.0 from the CCP4 monomer library *versus* 111.9° here) is noted, although based upon the density maps (Supplementary Figs. S2 and S3) the ligand does not appear to be misfitted. The NADPH nicotinamide group is responsible for hydride transfer to the FMN prosthetic group during the first part of the double-displacement enzymatic reaction (Saito *et al.*, 2008); owing to the absence of density for this moiety, the complete structural details of the *Pg*FabK catalytic mechanism cannot be fully elucidated. However, the adenine-ring system, the ribose ring and both the 2′- and 5′-phosphates have clear electron density, and this portion of the NADPH molecule is believed to be bound to the enzyme in its true binding conformation. The 2′-ribosyl phosphate group of NADPH is observed to make favorable electrostatic interactions with the positively charged Lys263 as well as the His46 residue, which is likely to be either positively charged or protonated on the N$^{\varepsilon}$ atom (Fig. 4). The corresponding residues in the NADH-binding *S. pneumoniae* FabK enzyme are Ala267 and Pro47, which may explain the difference in cofactor preference between these two enzymes. The adenine-ring system of the bound NADPH is observed to stack between His46 and Pro74 and to make favorable electrostatic binding interactions with both Glu75 and Tyr73. The distance of the NADPH adenosyl moiety from the FMN prosthetic group in the FabK active site would appear to allow correct placement of the missing nicotinamide moiety near the FMN isoalloxazine-ring system (Supplementary Fig. S4), lending further credence to the possibility that, although only partially resolved, the binding conformation of the NADPH fragment reflects the true binding conformation of the full NADPH molecule. Further studies are under way to confirm this hypothesis.

3.3. Insights into the enzyme mechanism

A comparison of the aligned sequences of FabK enzymes from three species for which the structures have been determined, *S. pneumoniae*, *Thermotoga maritima* and *P. gingivalis*, shows a high degree of similarity between the structures, with 43% overall identity between the *P. gingivalis* and *T. maritima* sequences and 41% overall identity between the *P. gingivalis* and *S. pneumoniae* sequences (Supplementary Fig. S5). The *T. maritima* and *S. pneumoniae* sequences have 49% overall identity. Across all three species, 34% of residues are identical overall, with the active-site similarity being significantly higher. Within a 4 Å region defined by the phenylimidazole-derivative FabK inhibitor in the *S. pneumoniae* co-crystal structure (Saito *et al.*, 2008), 42% of residues are identical across all three species, increasing to 58% if similarity (Val/Ala, Leu/Ile and Asp/Glu) is considered. Interestingly, most of the active-site differences are found in the *P. gingivalis*

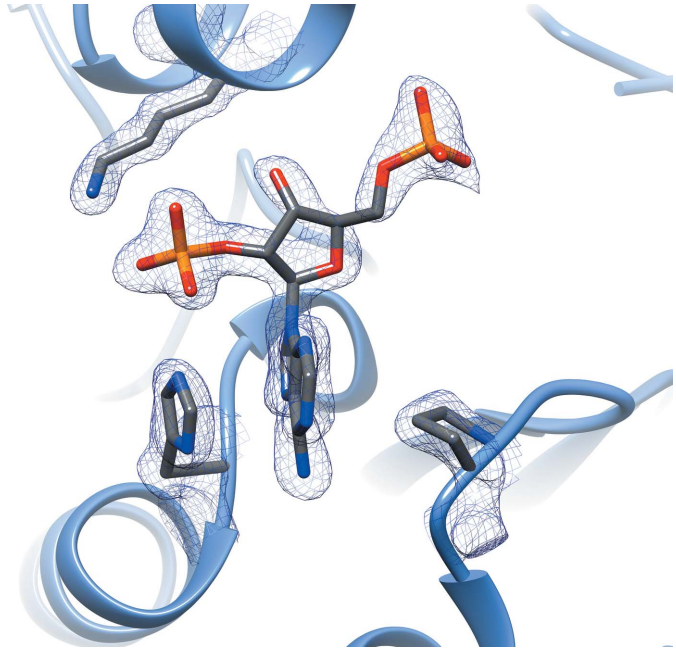

Figure 4
*Pg*FabK–NADPH interactions. $2F_o - F_c$ density map of the active-site NADPH fragment and interacting residues (shown at 1.25 r.m.s.d.).

protein; the *T. maritima* and *S. pneumonia* active sites are 90% similar. Notable differences in the *P. gingivalis* active site are Asn144 and Glu277, which differ significantly from the corresponding residues in the enzymes from the other two species. A highly conserved region from Ala188 to Phe195 corresponds to the FMN-binding region, which differs amongst all three species only by a methionine substitution in *Tm*FabK at the position corresponding to Val191.

An analysis of highly conserved residues in the FabK active site can provide some insight into the residues that are involved in the catalytic mechanism. A protein-family analysis based upon globally conserved residues reveals that the FabK enzyme falls in the nitronate monooxygenase (NMO; formerly 2-nitropropane dioxygenase) family of flavoproteins. Previous reports on the mechanism of NMO enzymes have suggested a role for an active-site histidine residue acting as a catalytic base in the oxidative reaction (Gadda & Francis, 2010; Francis & Gadda, 2008). Consistent with this, a globally conserved histidine residue (His143 in *P. gingivalis*) is located near the active site of the FabK enzyme as part of a structurally conserved GGH motif on loop 6 of the TIM-barrel structure. We suggest a possible role of the His residue as a proton donor/acceptor (catalytic acid/base) in the FabK reduction reaction, facilitating the reduction of FMN by the NADPH substrate and the subsequent reduction of the enoyl substrate by reduced FMN. Additionally, the globally conserved residues Trp21 located in loop 1 and Pro74 in loop 3 are adjacent to the NADPH-binding site discussed above and may play a functional role in facilitating the binding of the NADPH cofactor.

3.4. Role of the stringently required monovalent cations

The activity of the FabK enzyme has previously been reported to depend on the presence of a monovalent cation salt in the enzyme conditions, with ammonium chloride having the most potent effect (Marrakchi *et al.*, 2003). This effect has also been observed and reported for the *Pg*FabK enzyme (Hevener *et al.*, 2012). Furthermore, studies with the *Sp*FabK enzyme, including high-throughput screening, reported the use of ammonium chloride as the salt in the assay buffer (Ozawa *et al.*, 2007). This suggests a possible structural or catalytic role for the monovalent cation, although it is interesting to note that the order reported by Marrakchi and coworkers for the salt activation of enzymatic activity closely follows the Hofmeister series (Hofmeister, 1888). This may suggest an additional role of the monovalent cation salt in facilitating the solubility and stability of the protein.

In the structure reported here, a sodium ion was identified in the active site of the *Pg*FabK enzyme adjacent to the FMN-binding site (Fig. 5). This density was modelled as a sodium ion owing to the presence of a relatively high concentration of sodium in the storage and crystallization buffers, as well as the types of coordinating atoms and their distances from the metal. The sodium ion is coordinated by an active-site water (2.37 Å), the Glu136 OE2 atom (2.37 Å), the Asn144 OD1 atom (2.32 Å) and the Gly141 backbone carbonyl O atom

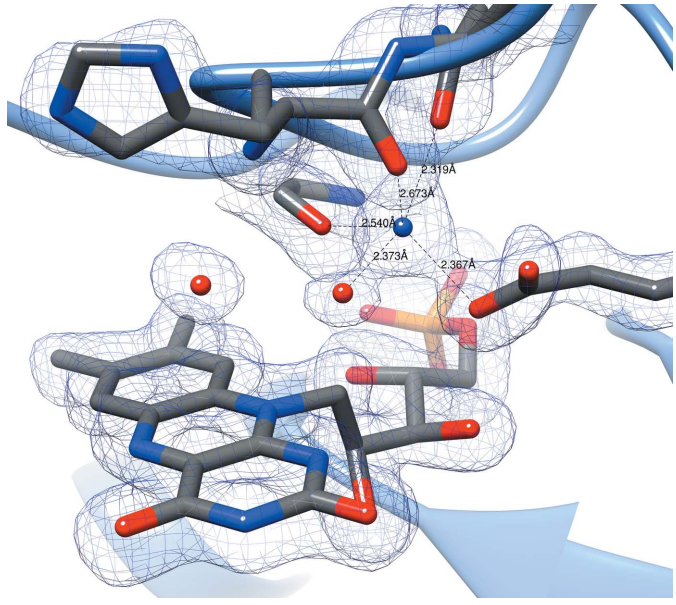

Figure 5
Sodium-ion coordination in the active site. The electron-density contour map at 1.25 r.m.s.d. shows approximately trigonal bipyramidal coordination of the sodium ion.

(2.54 Å). The His143 backbone carbonyl O atom also appears to play a coordinating role, although the distance is greater at 2.67 Å. The usual coordination number of monovalent cations such as sodium or potassium is five or six (trigonal bipyramidal or octahedral), while divalent cations prefer a coordination number of six (Harding *et al.*, 2010). Additionally, the normal cation-to-donor atom distance for sodium is 2.38–2.41 Å. The observed coordination of the sodium ion in this structure may in part explain the activation of this enzyme by monovalent cation salts, particularly ammonium chloride. The distances and geometries between the sodium cation and the coordinating atoms in the active-site residues suggest a five-point coordination (trigonal bipyramidal) of the sodium ion; however, the coordination is slightly distorted from the ideal trigonal bipyramidal geometry and the coordinating His134 O atom falls outside the typical cation-to-donor range. A four-point coordination, as would be seen with an NH_4^+ cation, may be more favorable as the tetragonal geometry would be less distorted. Further, the structure suggests that the six-point coordination (octahedral) that would be preferred by divalent cations could not be achieved, which may explain the negative effect on activity previously reported for divalent cation salts (Marrakchi *et al.*, 2003). Whether the active-site cation plays a catalytic role or simply a structural role remains to be determined.

4. Conclusions

FabK (enoyl-ACP reductase II) is a novel antimicrobial target in the bacterial fatty-acid synthesis pathway. As the sole enoyl reductase enzyme in *P. gingivalis*, a major causative organism of chronic periodontitis, FabK has strong potential for

development as a drug target. Using X-ray crystallographic methods, we have identified conditions leading to crystals which diffracted to high resolution and we determined the *Pg*FabK crystal structure at 1.9 Å resolution. This FabK structure is the first in which all flexible loops are fully resolved and the binding site, with the FMN prosthetic group and a partially resolved NADPH cofactor, is visible. The results of these studies have improved our understanding of the FabK target with respect to the role of the cofactor and the monovalent cation in the catalytic mechanism and will facilitate future rational drug-discovery efforts targeting this enzyme.

5. Related literature

The following reference is cited in the Supporting Information for this article: Bell *et al.* (2012).

Funding information

Funding was provided by NIDCR 5T32-DE018381, UIC College of Dentistry, MOST Program. Use of LS-CAT Sector 21 was supported by the Michigan Economic Development Corporation and the Michigan Technology Tri-Corridor for the support of this research program (grant 085P1000817). Use of the Advanced Photon Source was supported by the US Department of Energy, Office of Science, Office of Basic Energy Sciences under Contract No. DE-AC02-11357.

References

Bell, J. A., Cao, Y., Gunn, J. R., Day, T., Gallicchio, E., Zhou, Z., Levy, R. & Farid, R. (2012). *International Tables for Crystallography*, Vol. *F*, edited by E. Arnold, D. M. Himmel & M. G. Rossmann, pp. 534–538, https://doi.org/10.1107/97809553602060000864. Chester: International Union of Crystallography.

Blinkhorn, A., Bartold, P. M., Cullinan, M. P., Madden, T. E., Marshall, R. I., Raphael, S. L. & Seymour, G. J. (2009). *Br. Dent. J.* **207**, 117–125.

Chávarry, N. G., Vettore, M. V., Sansone, C. & Sheiham, A. (2009). *Oral Health Prev. Dent.* **7**, 107–127.

Chen, V. B., Arendall, W. B., Headd, J. J., Keedy, D. A., Immormino, R. M., Kapral, G. J., Murray, L. W., Richardson, J. S. & Richardson, D. C. (2010). *Acta Cryst.* D**66**, 12–21.

Emsley, P., Lohkamp, B., Scott, W. G. & Cowtan, K. (2010). *Acta Cryst.* D**66**, 486–501.

Fitzpatrick, S. G. & Katz, J. (2010). *J. Dent.* **38**, 83–95.

Francis, K. & Gadda, G. (2008). *Biochemistry*, **47**, 9136–9144.

Gadda, G. & Francis, K. (2010). *Arch. Biochem. Biophys.* **493**, 53–61.

Gerusz, V. (2010). *Annu. Rep. Med. Chem.* **45**, 295–311.

Gerusz, V. *et al.* (2012). *J. Med. Chem.* **55**, 9914–9928.

Hajishengallis, G., Liang, S., Payne, M. A., Hashim, A., Jotwani, R., Eskan, M. A., McIntosh, M. L., Alsam, A., Kirkwood, K. L., Lambris, J. D., Darveau, R. P. & Curtis, M. A. (2011). *Cell Host Microbe*, **10**, 497–506.

Harding, M. M., Nowicki, M. W. & Walkinshaw, M. D. (2010). *Crystallogr. Rev.* **16**, 247–302.

Hevener, K. E., Mehboob, S., Boci, T., Truong, K., Santarsiero, B. D. & Johnson, M. E. (2012). *Protein Expr. Purif.* **85**, 100–108.

Hofmeister, F. (1888). *Arch. Exp. Pathol. Pharmakol.* **24**, 247–260.

Joshipura, K., Zevallos, J. C. & Ritchie, C. S. (2009). *Compend. Contin. Educ. Dent.* **30**, 430–439.

Kabsch, W. (2010*a*). *Acta Cryst.* D**66**, 125–132.

Kabsch, W. (2010*b*). *Acta Cryst.* D**66**, 133–144.

Kingry, L. C., Cummings, J. E., Brookman, K. W., Bommineni, G. R., Tonge, P. J. & Slayden, R. A. (2013). *J. Bacteriol.* **195**, 351–358.

Krissinel, E. & Henrick, K. (2007). *J. Mol. Biol.* **372**, 774–797.

Lovegrove, J. M. (2004). *J. N. Z. Soc. Periodontol.*, pp. 7–21.

Marrakchi, H., DeWolf, W. E. Jr, Quinn, C., West, J., Polizzi, B. J., So, C. Y., Holmes, D. J., Reed, S. L., Heath, R. J., Payne, D. J., Rock, C. O. & Wallis, N. G. (2003). *Biochem. J.* **370**, 1055–1062.

McCoy, A. J., Grosse-Kunstleve, R. W., Adams, P. D., Winn, M. D., Storoni, L. C. & Read, R. J. (2007). *J. Appl. Cryst.* **40**, 658–674.

Murshudov, G. N., Skubák, P., Lebedev, A. A., Pannu, N. S., Steiner, R. A., Nicholls, R. A., Winn, M. D., Long, F. & Vagin, A. A. (2011). *Acta Cryst.* D**67**, 355–367.

Oppermann, U., Filling, C., Hult, M., Shafqat, N., Wu, X., Lindh, M., Shafqat, J., Nordling, E., Kallberg, Y., Persson, B. & Jörnvall, H. (2003). *Chem. Biol. Interact.* **143–144**, 247–253.

Ozawa, T., Kitagawa, H., Yamamoto, Y., Takahata, S., Iida, M., Osaki, Y. & Yamada, K. (2007). *Bioorg. Med. Chem.* **15**, 7325–7336.

Pettersen, E. F., Goddard, T. D., Huang, C. C., Couch, G. S., Greenblatt, D. M., Meng, E. C. & Ferrin, T. E. (2004). *J. Comput. Chem.* **25**, 1605–1612.

Saito, J., Yamada, M., Watanabe, T., Iida, M., Kitagawa, H., Takahata, S., Ozawa, T., Takeuchi, Y. & Ohsawa, F. (2008). *Protein Sci.* **17**, 691–699.

Saito, J., Yamada, M., Watanabe, T., Kitagawa, H. & Takeuchi, Y. (2006). *Acta Cryst.* F**62**, 576–578.

Schaudinn, C., Gorur, A., Keller, D., Sedghizadeh, P. P. & Costerton, J. W. (2009). *J. Am. Dent. Assoc.* **140**, 978–986.

Snowden, C. B., Miller, T. R., Jensen, A. F. & Lawrence, B. A. (2003). *Public Health Rep.* **118**, 10–17.

Vered, Y., Zini, A., Mann, J., DeVizio, W., Stewart, B., Zhang, Y. P. & Garcia, L. (2009). *J. Clin. Dent.* **20**, 62–65.

White, S. W., Zheng, J., Zhang, Y.-M. & Rock, C. O. (2005). *Annu. Rev. Biochem.* **74**, 791–831.

Winn, M. D. *et al.* (2011). *Acta Cryst.* D**67**, 235–242.

Wu, J. T., Wu, L. H. & Knight, J. A. (1986). *Clin. Chem.* **32**, 314–319.